

Excited-State Energy Surfaces in Molecules Revealed by Impulsive Stimulated Raman Excitation Profiles

Giovanni Batignani,* Carlotta Sansone, Carino Ferrante, Giuseppe Fumero, Shaul Mukamel, and Tullio Scopigno*

Cite This: *J. Phys. Chem. Lett.* 2021, 12, 9239–9247

Read Online

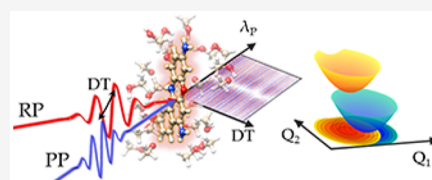
ACCESS |

Metrics & More

Article Recommendations

Supporting Information

ABSTRACT: Photophysical and photochemical processes are ruled by the interplay between transient vibrational and electronic degrees of freedom, which are ultimately determined by the multidimensional potential energy surfaces (PESs). Differences between ground and excited PESs are encoded in the relative intensities of resonant Raman bands, but they are experimentally challenging to access, requiring measurements at multiple wavelengths under identical conditions. Herein, we perform a two-color impulsive vibrational scattering experiment to launch nuclear wavepacket motions by an impulsive pump and record their coupling with a targeted excited-state potential by resonant Raman processes with a delayed probe, generating in a single measurement background-free vibrational spectra across the entire sample absorption. Building on the interference between the multiple pathways resonant with the excited-state manifold that generate the Raman signal, we show how to experimentally tune their relative phase by varying the probe chirp, decoding nuclear displacements along different normal modes and revealing the multidimensional PESs. Our results are validated against time-dependent density functional theory.



The investigation of light-induced processes is essential for the understanding of a variety of complex phenomena at the interface between physics, chemistry, and biology, in which excited-state dynamics causes the transient modification of molecular properties and atomic configurations. The latter are ultimately determined by the multidimensional potential energy surfaces (PESs) describing how the excited-state potential changes along the different normal modes.¹ Spontaneous Raman spectroscopy plays a pivotal role for accessing the vibrational fingerprints of solid-state systems or complex molecular compounds. Tuning the excitation of the Raman pulse in resonance with an electronic transition enables selective enhancement of the Raman cross section.² Because the resonance Raman (RR) cross section depends on the displacement between ground and excited potential energy surfaces along the normal coordinates, the relative intensities of the measured RR bands encode information on the potential energy surfaces. Critically, in order to extract such molecular information, several spectra have to be recorded scanning the Raman pump wavelength across the absorption profile, performing a sequence of measurements at multiple wavelengths under identical conditions, and with the detection of the experimental signals that is typically hampered by the overwhelming fluorescent background. Most importantly, spontaneous Raman spectroscopy can provide only differential information on excited-state geometries relative to the equilibrium configuration on the ground state.

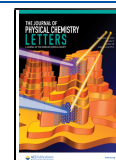
Herein, we introduce a method to determine the nuclear displacements between different PESs, based on an impulsive stimulated Raman scattering (ISRS) experiment, circumventing the limitations of spontaneous Raman spectroscopy.

ISRS exploits the joint action of two ultrashort laser fields to measure vibrational excitations in the time domain.^{3–5} A femtosecond Raman pump (RP) coherently stimulates nuclear wavepackets of Raman active modes,^{6,7} which modulate the transmissivity of the sample and are detected by monitoring the transmission of a temporally delayed probe pulse (PP) as a function of the time delay ΔT between the RP–PP pair: Fourier transforming over ΔT enables retrieving the Raman information in the frequency domain.^{8,9} Because the ISRS spectra are recorded for temporally separated Raman and probe fields, the experimental signals are not affected by nonlinear background processes generated during the overlap of the ultrashort pulses, which in contrast can plague frequency domain coherent Raman techniques.^{10–14} In addition, thanks to the heterodyne detection, the vibrational information is engraved on the PP; hence, the fluorescence and the incoherent background signals are efficiently suppressed. Importantly, when the Raman pulse is longer than the period of a normal mode, it cannot efficiently stimulate vibrational coherences, making ISRS less effective in probing high energetic modes. In order to isolate the vibrational fingerprints on the initially populated electronic level, we employ a two-color ISRS experimental configuration, with an off-resonant

Received: July 9, 2021

Accepted: August 16, 2021

Published: September 17, 2021



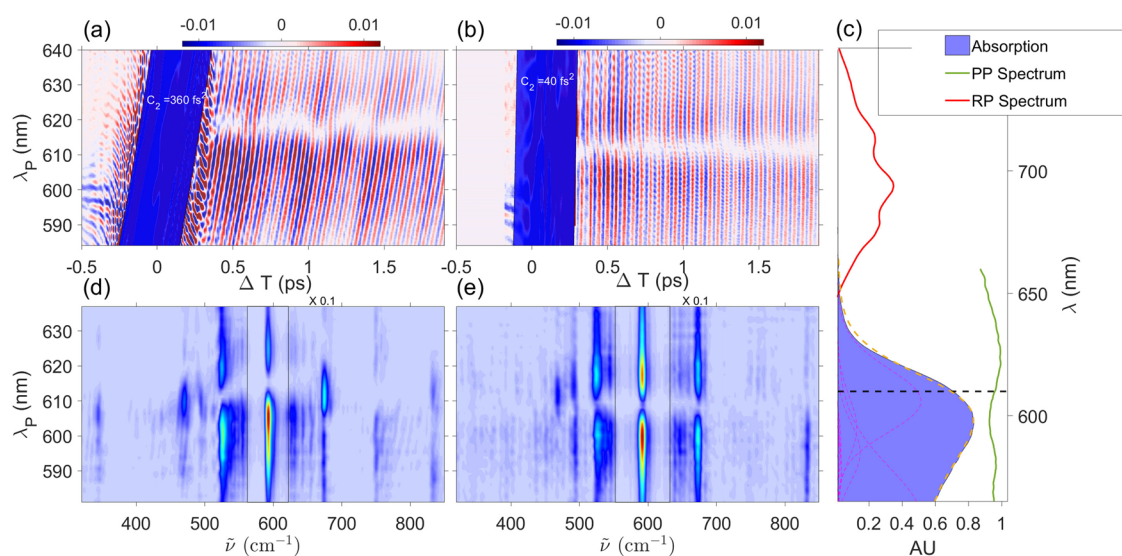


Figure 1. Broadband two-color ISRS spectra of cresyl violet recorded in the time domain (top panels, a and b) as a function of the probe wavelength λ_p and the RP–PP relative delay ΔT , acquired for two different values of the probe chirp (360 and 40 fs²). The blue box marks the region covered by the coherent artifact. The corresponding spectra in the frequency domain (d and e) can be obtained by truncating the coherent artifact and Fourier transforming over ΔT and are reported in the bottom panels as a function of the wavenumber $\tilde{\nu}$ (the central region around 592 cm⁻¹ has been scaled by a factor 0.1 to enhance the visibility of the weaker Raman modes). The absorption spectrum of the methanol dissolved sample is shown in the right panel (c) with the RP and PP spectral profiles and is compared with the one (yellow dashed line) simulated from the molecular parameters reported in Table 1. Low (300 cm⁻¹) and a high (1400 cm⁻¹) frequency contributions have been included in the simulation, taking into account low-frequency contributions with vanishing polarizability derivative not stimulated by the nonresonant pump and the high-frequency modes out of reach for the ISRS technique. The contributions originated by the vibronic progression are reported as magenta lines. The black dashed line indicates the transition to the vibrationally ground level of the excited electronic state.

Raman pulse E_R and a broadband probe E_p , which covers the molecular response across its absorption profile, enabling the study of the couplings with a targeted electronically excited level, by monitoring the frequency-dispersed ISRS signal as a function of the probe wavelength λ_p . We demonstrate how to assign the complex dependence (as a function of λ_p) of the measured mode-dependent Raman excitation profiles to the corresponding nuclear displacements. The relative intensities of the ISRS modes are studied, including chirp effects, which can critically modulate the amplitude of the time domain Raman response even in the fully off-resonance regime.^{15,16} The addition of an actinic pump, temporally longer than the period of the normal modes under investigation, to the scheme proposed here allows photoexcitation of the sample on a targeted electronic level^{17–22} without promoting vibrational coherences. Hence, because of the femtosecond resolution probing of the RP–PP pair,^{23–27} probing the ISRS response across the excited-state absorption activated upon the photoexcitation enables the extension to the mapping of the relative orientation and displacements between arbitrary excited transient PESs. Within such a scheme the RP may be tuned in resonance with the stimulated emission to enhance the ISRS cross section. The measurement of excited-state orientations by ISRS offers the chance to map complex PESs and to identify the vibrational degrees of freedom responsible for the ultrafast relaxation of the system along excited-state potentials, as in the presence of dynamic Stokes shift,²⁸ where measuring the time-dependent REPs would offer the chance to follow the photoexcited chromophore PES relaxation along the involved vibrational degrees of freedom, or photoinduced charge-transfer events.²⁹

The two-color ISRS response is measured for cresyl violet (CV)^{30–34} dissolved in methanol, a highly fluorescent oxazine

dye with a long-lived excited electronic state. Because of the strong fluorescence background, with a small (~ 500 cm⁻¹) Stokes shift, the CV spontaneous resonant Raman response cannot be explored around the system absorption profile and can be obtained only at excitation wavelengths far to the blue side of the absorption maximum.³¹ Hence, CV represents an ideal candidate for testing the capabilities of our two-color ISRS setup. Our experimental results are reported in Figure 1: the temporal traces recorded in the time domain are shown in the top panels (a and b) for two values of the probe chirp C_2 (360 fs² and 40 fs²), while the corresponding spectra in the frequency domain, obtained upon truncating the coherent artifact (highlighted by the blue boxes) and fast Fourier transforming (FFT), are reported in the bottom panels (d and e). Because the ISRS signal is dominated by the mode centered at 592 cm⁻¹, the spectral region around the 592 cm⁻¹ peak has been scaled by a factor 0.1 in order to enhance the visibility of the other weaker Raman bands (at 345, 470, 493, 526 675, 752, and 833 cm⁻¹). It is worth stressing that in view of the nonresonant nature of the Raman pump employed in the present scheme, only the Raman modes with a nonvanishing polarizability derivative can be efficiently stimulated. As expected, the amplitude of the ISRS oscillations is enhanced around the sample absorption profile, which is reported in Figure 1c. The intensities of the different Raman peaks show complex profiles, which vary as a function of the PP wavelength and depend on both PP chirp as well as on the specific Raman mode under consideration. For example, the 592 cm⁻¹ mode shows a maximum intensity slightly red-shifted with respect to the absorption maximum for $C_2 = 360$ fs² and turns to a broad bilobed profile for $C_2 = 40$ fs². In contrast, the 525 cm⁻¹ mode shows similar bilobed profiles for both $C_2 = 40$ fs² and $C_2 = 360$ fs². The traces in the time domain reveal a π

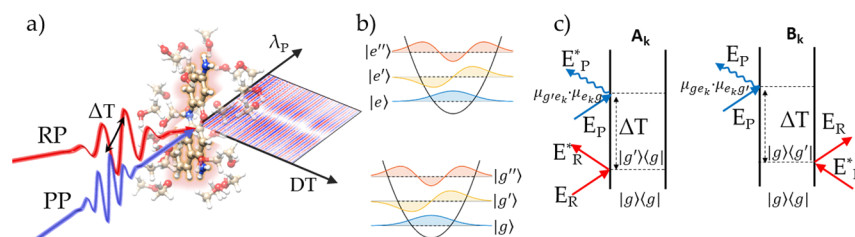


Figure 2. Sketch of the two-color ISRS experimental setup used in this work (a). The electronic and vibrational levels involved in the generation of the measured signal are reported in panel b: the vibrational progression on the ground electronic state is indicated as $|g\rangle$, $|g'\rangle$, $|g''\rangle$, while the corresponding manifold in the electronic excited state is termed $|e\rangle$, $|e'\rangle$, $|e''\rangle$. The Feynman diagrams describing the ISRS process are reported in panel c.

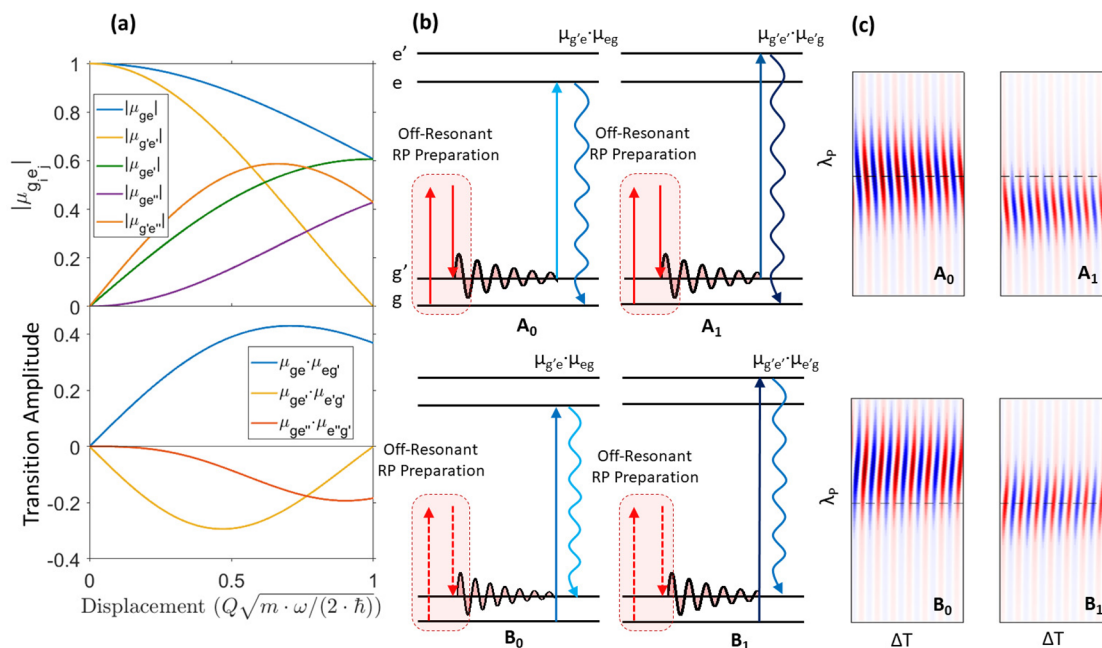


Figure 3. (a) Transition dipole moments as a function of the dimensionless displacement along the normal modes. In the top panel the absolute value of single transition dipole moments are shown (the vibrational progression on the ground electronic state is indicated as $|g\rangle$, $|g'\rangle$; the corresponding manifold in the electronic excited state is termed $|e\rangle$, $|e'\rangle$, $|e''\rangle$), while in the bottom panel we report the intensity factors associated with the various ISRS pathways shown in panel b. Each factor corresponds to the product of two dipole moments. The corresponding signals in the time domain are reported in panel c, with the horizontal dashed line indicating the PP wavelength matching the e–g transition.

phase shift between the oscillations red and blue-shifted with respect to the node with vanishing signal.

To interpret this complex behavior and extract structural information from the measurements of mode-dependent intensity profiles in CV, we studied the role of the resonant PP chirp and detection wavelength in the generation of the nonlinear signal. The third-order nonlinear polarization associated with the ISRS process can be evaluated through a perturbative expansion of the molecular density matrix in powers of the electric fields $E_{R/P} = E_{R/P}^0(t)e^{-i\omega_{R/P}t} + \text{c.c.}$, and the different pathways that contribute to the total response can be identified by taking advantage of a diagrammatic approach.^{6,35–38} Considering the pulse scheme and the energy levels reported in Figure 2a,b, with vibrational manifolds in the electronic ground and resonant excited state indicated as $|g\rangle$, $|g'\rangle$, ... and $|e\rangle$, $|e'\rangle$, ..., respectively, the Feynman diagrams that take into account the system response are shown in Figure 2c. Because the RP is tuned off resonant with respect to the sample absorption, it selectively generates vibrational coherences only in the initially populated electronic level, the ground state in the present case ($|g'\rangle$ $\langle g|$ and $|g\rangle\langle g'|$ states,

corresponding to diagrams A_k and B_k , respectively). Then the system evolves unperturbed until an interaction with the PP and a free induction decay (that leaves the system in a population state) enabling us to probe the vibrational coherences after the tunable time delay ΔT . Importantly, while in the off-resonant PP regime the state e is a virtual level and A_k – B_k destructively interfere resulting in small or vanishing signals,¹⁵ in the resonant case the ket side of the density matrix is promoted to the excited state and, taking advantage of the broadband nature of the PP, it can be projected to the entire vibrational manifold, with a distribution ruled by the transition dipole moments $\mu_{nm} = \langle \psi_n | \hat{\mu} | \psi_m \rangle$. Assuming the Condon approximation,^{22,39} the intensities of the transition dipole moments are determined by the Franck–Condon (FC) factors and can be evaluated by computing the FC overlap integrals between the initial and final vibrational wave functions $\mu_{g'e_k} = \langle g_j | e_k \rangle$, which depend on the displacement of the PES along the considered normal mode. We adopt the harmonic approximation for the molecular potentials, according to which the vibrational wave functions are expressed by products of orthogonal shifted harmonic

oscillators. In the left panel of Figure 3, we report some values of the transition dipole moments as a function of the dimensionless displacement factor $d = Q\sqrt{\frac{m\omega_0}{2\hbar}}$.

The third-order polarizations, $P_{A_g}^{(3)}(\omega, \Delta T)$ and $P_{B_g}^{(3)}(\omega, \Delta T)$, taking into account the signal induced by a given vibrational mode g' , can be directly computed from the diagrams in Figure 2 and are^{40,41}

$$P_{A_g}^{(3)}(\omega, \Delta T) = \sum_{e_k} \frac{\mu_{g'e_k} \mu_{e_k g'}}{\hbar^3} \int_{-\infty}^{+\infty} \int_{-\infty}^{+\infty} d\Delta d\omega_D \frac{I_{RA}(\Delta, \Delta T) E_p(\omega - \Delta) G(\omega_D)}{(\Delta - \tilde{\omega}_{g'g})(\omega - \tilde{\omega}_{e_k g'} - \omega_D)} \quad (1)$$

and

$$P_{B_g}^{(3)}(\omega, \Delta T) = \sum_{e_k} \frac{\mu_{g'e_k} \mu_{e_k g'}}{\hbar^3} \int_{-\infty}^{+\infty} \int_{-\infty}^{+\infty} d\Delta d\omega_D \frac{I_{RB}(\Delta, \Delta T) E_p(\omega + \Delta) G(\omega_D)}{(-\Delta - \tilde{\omega}_{g'g})(\omega - \tilde{\omega}_{e_k g'} - \omega_D)} \quad (2)$$

$\tilde{\omega}_{ij} = \omega_j - i\gamma_{ij}$, $\omega_{ij} = \omega_i - \omega_j$ indicates the energy difference between i - j levels; Δ is an integration variable (with the maximum contribution centered at $\tilde{\omega}_{g'g}$); $G(\omega_D)$ is the inhomogeneous broadening Gaussian function, and $\gamma_{ij} = \tau_{ij}^{-1}$ is the dephasing rate of the $|i\rangle$ $|j\rangle$ coherence. The $I_{RA}(\Delta, \Delta T)$ and $I_{RB}(\Delta, \Delta T)$ terms in eqs 1 and 2 represent the preparation function of the $|g'\rangle$ $|g\rangle$ and $|g\rangle$ $|g'\rangle$ vibrational coherences generated by the Raman pulse, and under off-resonant RP excitation, they are purely real functions. Importantly, Raman modes with a period much shorter than the pump duration will exhibit an inefficient stimulation of the vibrational coherences, resulting in small amplitudes of the ISRS peaks.⁵ The summation over e_k in eqs 1 and 2 takes into account the PES one-dimensional projection on the g' vibrational subspace, and in order to retrieve the desired total nonlinear polarization of the system, eqs 1 and 2 should be summed over all the g' ground-state normal modes under consideration, according to

$$P_{A/B}^{(3)}(\omega, \Delta T) = \sum_{g'} P_{A_g'/B_g'}^{(3)}(\omega, \Delta T)$$

Details on the derivation of eqs 1 and 2 and expressions for the $I_{RA}(\Delta, \Delta T)$ and $I_{RB}(\Delta, \Delta T)$ functions are reported in the Supporting Information. For simplicity, the calculation can be performed assuming that the central frequency ω_p of the chirped probe pulse arrives at $t = 0$ and that the RP is centered at $t = -\Delta T$ (i.e., shifted at negative time delays and preceding the PP). Under such assumptions the RP-PP fields of eqs 1 and 2 can be expressed in the frequency domain as

$$E_R(\omega) = E_R^{(0)}(\omega) \exp(-i\omega_R \Delta T), \\ E_p(\omega) = E_p^{(0)}(\omega) \exp[i \sum_n C_n (\omega - \omega_p)^n] \quad (3)$$

where $E_{R/P}^{(0)}(\omega)$ are positive real functions representing the square root of the RP-PP spectra; C_2 is the group delay dispersion taking into account the linear chirp of the PP, and C_n indicates the n th higher-order dispersion terms.

When the PP does not vary across the sample, the third-order nonlinear polarization, which depends on the PP temporal and spectral profile, is constant and hence the ISRS responses $S(\omega, \Delta T) - S(\omega, \Omega)$, in the time and frequency domains, respectively, can be calculated as

$$S(\omega, \Delta T) \propto -\Im\{[P_A^{(3)}(\omega) + P_B^{(3)}(\omega)]E_p^{(0)*}(\omega)\}$$

$$S(\omega, \Omega) = \int_{-\infty}^{+\infty} d\Delta T e^{+i\Omega \Delta T} S(\omega, \Delta T)$$

where $\Im(f)$ indicates the imaginary part of f .

However, we note that, because of the absorption of the E_p field during its propagation, the polarizations $P_A^{(3)}(\omega)$ and $P_B^{(3)}(\omega)$ are not constant and decay along the beam path within the sample. For this reason, a quantitative evaluation of the ISRS signal requires us to numerically integrate the PP spectral profile over the sample length, by using the coupled wave equations^{10,42}

$$\begin{cases} \frac{\partial E_p(\omega, z)}{\partial z} = \frac{i\omega}{c} [P_A^{(3)}(z, \omega) + P_B^{(3)}(z, \omega)] - \frac{\alpha(\omega)}{2} E_p(\omega, z) \\ P_A^{(3)}(z, \omega) = \sum_{e_k} \frac{\mu_{g'e_k} \mu_{e_k g'}}{\hbar^3} \int_{-\infty}^{+\infty} \int_{-\infty}^{+\infty} d\Delta d\omega_D \frac{I_{RA}(\Delta) E_p(\omega - \Delta, z) G(\omega_D)}{(\Delta - \tilde{\omega}_{g'g})(\omega - \tilde{\omega}_{e_k g'} - \omega_D)} \\ P_B^{(3)}(z, \omega) = \sum_{e_k} \frac{\mu_{g'e_k} \mu_{e_k g'}}{\hbar^3} \int_{-\infty}^{+\infty} \int_{-\infty}^{+\infty} d\Delta d\omega_D \frac{I_{RB}(\Delta) E_p(\omega + \Delta, z) G(\omega_D)}{(-\Delta - \tilde{\omega}_{g'g})(\omega - \tilde{\omega}_{e_k g'} - \omega_D)} \end{cases} \quad (4)$$

where $\alpha(\omega)$ indicates the frequency dependent attenuation coefficient. The ISRS signal $S(\omega, \Delta T)$ in the time domain can be finally evaluated as the normalized difference between the transmitted PP spectrum in the presence and in the absence of the RP induced nonlinear polarization.

To interpret the experimental results it is worth considering separately the different pathways, contributing to the e_k summations (eqs 1–4), that generate the polarizations P_A and P_B . From a diagrammatic perspective, this is equivalent to recasting the Feynman diagrams shown in Figure 2c to the corresponding ones in the energy level scheme, which are reported in Figure 3b (we have explicitly shown only the e and e' vibrational levels in the electronic excited state). Diagrams in Figure 3b help to directly visualize the spectral components of the Raman and probe fields contributing to the experimental signal generation at a given PP wavelength. Importantly, at odds with fully nonresonant ISRS processes, where the total response of the system is generated by the interference between pathways involving interactions with different probe pulse spectral components (red-shifted and blue-shifted with respect to the probed wavelength),^{16,40,43} in the resonant case the signal at a given probe wavelength is generated by the interference between processes which share interactions with the same probe color, but with a different state in the excited-state manifold, hence encoding information on the nuclear displacements between different potential energy surfaces. In particular, the A_0/A_1 processes are generated from an interaction with a PP component red-shifted by one vibrational quantum with respect to the probed wavelength and originate from the transitions $e \rightarrow g$ and $e' \rightarrow g$, hence resulting in contributions centered at ω_{eg} and $\omega_{e'g}$, respectively. In contrast, B_0 and B_1 generate contributions centered around $\omega_{eg'}$ and $\omega_{e'g'}$ and originate from interactions with spectral components of the PP blue-shifted with respect to the probed wavelengths. Interestingly, while A_0 and B_0 generate an ISRS response centered at different PP wavelengths, they originate from quantum pathways involving the same excited state e , resulting in ISRS signals oscillating in phase with each other (Figure 3c).

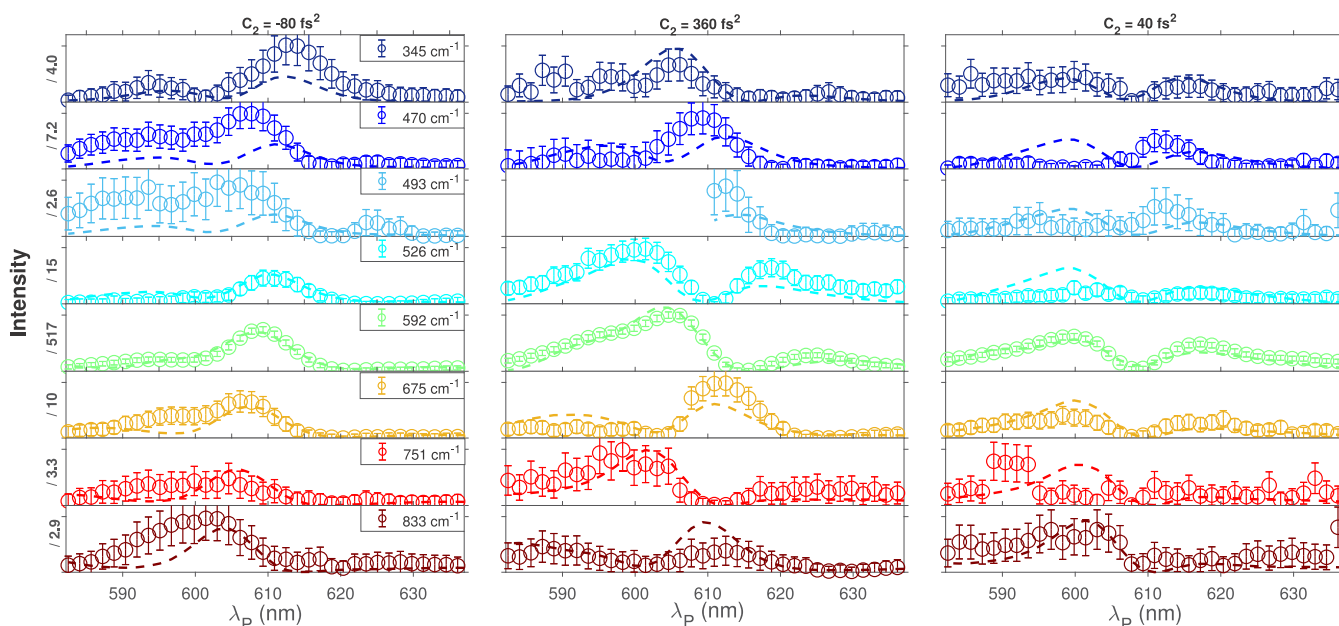


Figure 4. Normalized cresyl violet ISRS Raman excitation profiles measured for different vibrational modes. The REP intensities have been obtained by fitting the frequency domain traces (Figure 1d,e) with a sum of Lorentzian profiles, evaluating the areas of the different Raman bands. The data (circles) and the model (solid lines) are compared as a function of the λ_p probe pulse wavelength for three different values of the probe chirp (reported on top of each column). All the y-axes range from 0 to 1.2, and the absolute intensities of each mode have been scaled by the factors reported on the axis.

In contrast, both A_0 and B_1 generate an ISRS response centered at the same transition frequency (ω_{eg}). However, the amplitude of the corresponding oscillations is ruled by different dipole moments, namely, $\mu_{g'e'eg}$ for A_0 and $\mu_{g'e'e'g}$ for B_1 . Critically, as shown in Figure 3a, $\mu_{g'e'eg}$ and $\mu_{g'e'e'g}$ have opposite signs, and hence, they result in a destructive interference between the A_0 and B_1 processes. This elucidates the vanishing ISRS amplitude observed at the transition frequency ω_{eg} in Figure 1b,e. Similarly, the relative sign between the A_1 and B_0 processes, red and blue-shifted by one vibrational quantum with respect to the eg transition, rationalizes the π phase shift observed in the time domain traces around the node (Figure 1a,b). It is worth stressing that the interference between A_0 and B_1 pathways can strongly affect the detection of the Raman modes with small displacements between ground and excited PESs, i.e., the weakest Raman modes. In fact, as shown in the bottom panel of Figure 3a, for a small displacement ($d \lesssim 0.25$), the $\mu_{g'e'eg}$ and $\mu_{g'e'e'g}$ transition amplitudes are close in absolute value to each other. A convenient way to avoid the destructive interference between different quantum pathways can be derived from the observation that A_0 and B_1 are generated by interactions with different PP spectral components (red and blue separated by one vibrational quantum, with respect to the probed wavelength), which therefore can be shifted in time, introducing a chirp in the PP. For a linearly chirped PP, the arrival time of a given frequency ω varies as $t = 2C_2(\omega - \omega_p)$. The effective detection times of the vibrational coherences are equal to the average between the arrival times of the two PP frequencies involved in the nonlinear process, and hence, they correspond to $t_{\text{eff}}^A(\omega) = 2C_2\left(\omega - \omega_p - \frac{\omega_{k,g}}{2}\right)$, $t_{\text{eff}}^B(\omega) = 2C_2\left(\omega - \omega_p + \frac{\omega_{k,g}}{2}\right)$, respectively. This delay introduces a relative phase between the A_k and B_k processes, equal to $\Delta\phi_{B-A}$

$= \omega_{g'e'}(t_{\text{eff}}^B(\omega) - t_{\text{eff}}^A(\omega)) = 2C_2\omega_{g'g}^2$, which can be experimentally tuned by means of the probe chirp.

The above analysis clarifies that a wealth of information on the excited-state potentials is encoded in the dependence of the ISRS signal on the probe wavelength. This dependence is complicated by multiple interfering optical processes but can be controlled by varying the chirp of the PP. Following this strategy, we determined the nuclear displacements between the ground and excited PESs from the measured, mode-dependent Raman excitation profiles (REPs), i.e., the change in the intensities of the individual ISRS bands as a function of the probe wavelength. In Figure 4, we report the cresyl violet REP $S(\lambda_p, \tilde{\nu}_j)$ for different Raman modes ($\tilde{\nu}_j = 345, 470, 493, 525, 592, 675, 751, \text{ and } 832 \text{ cm}^{-1}$). $S(\lambda_p, \tilde{\nu}_j)$ have been extracted by fitting the ISRS maps in the frequency domain (Figure 1d,e) as the sum of Lorentzian profiles, which have been used to preliminarily identify the normal-mode frequencies. The REPs have been evaluated for three different values of the probe chirp ($-80, 40, \text{ and } 360 \text{ fs}^2$) to tune the relative phase between A_0 – B_1 processes: the experimental results are in good agreement with signals modeled using eqs 1–4, which have been numerically integrated using small steps of $dz = 12.5 \mu\text{m}$, considering the sample absorption and the nonlinear contributions separately.¹⁰ Because the $S(\lambda_p, \tilde{\nu}_j)$ signal is evaluated over a broad spectral range, the PP chirp has been included in the simulation considering also the third-order dispersion coefficient C_3 (details on the calibration are reported in Methods and in the Supporting Information). In order to retrieve the displacements of the excited PES along the normal modes, eqs 1–4 have been used to fit the experimental $S(\lambda_p, \tilde{\nu}_0)$ traces globally over the data sets measured at different PP chirps, considering fixed normal-mode frequencies and dephasing times. The obtained normal-mode frequencies $\tilde{\nu}_{g'g}$ and displacements $d = Q\sqrt{\frac{m\omega_0}{2\hbar}}$ are

summarized in Table 1, while the projection of ground- and excited-state potentials along two normal modes (592 and 675

Table 1. Peak Positions and Displacements between Ground- and Excited-State PESs Extracted by Fitting the ISRS Raman Excitation Profiles Reported with the Corresponding 90% Confidence Intervals^a

| $\tilde{\nu}_{g'g}$ (cm ⁻¹) | $d = Q\sqrt{\frac{m\omega_0}{2\hbar}}$ (DFT) | $d = Q\sqrt{\frac{m\omega_0}{2\hbar}}$ (experimental) | Q (au) |
|---|--|---|--------|
| 345 (2) | 0.27 | 0.18 (0.03) | 0.063 |
| 470 (2) | 0.24 | 0.21 (0.04) | 0.059 |
| 493 (2) | 0.13 | 0.15 (0.03) | 0.040 |
| 526 (2) | 0.18 | 0.26 (0.03) | 0.071 |
| 592 (2) | 0.60 | 0.63 (0.04) | 0.13 |
| 675 (2) | 0.19 | 0.19 (0.03) | 0.044 |
| 752 (2) | 0.11 | 0.17 (0.03) | 0.039 |
| 833 (2) | 0.17 | 0.17 (0.03) | 0.041 |

^aThe results are compared with the displacements obtained by TD-DFT calculations performed with CAM-B3LYP functional and the 6-311++G(2d,2p) basis set. In the last column the extracted detected displacements are reported in atomic units.

cm⁻¹) are reported in Figure 5. Importantly, our results indicate a high displacement ($d = 0.64 \pm 0.04$) of the excited PES along the 592 cm⁻¹ coordinate, pointing to an elongation of the Oxazine ring in the excited state (Figure 5), due to a reorganization of the electronic density in the excited state (as confirmed by the electronic density difference map reported in the Supporting Information as Figure S5), and small d (≤ 0.25) along the other investigated vibrational degrees of freedom. We note that the values reported in Table 1 are lower than the displacements obtained by spontaneous Raman spectroscopy for CV dissolved in water,³¹ as expected in view of the asymmetrically blue-shifted absorption spectrum of the aqueous CV solutions (reported in the Supporting Information). In Figure 1c, we show a comparison between the measured sample absorption spectrum and the one calculated using the ISRS retrieved displacement, where two additional contributions (at 300 and 1400 cm⁻¹), which take into account for the Raman mode not accessed by the present ISRS experiment, have been included in the simulation to fit the

experimental data. Interestingly, such a comparison indicates that CV has high-frequency displaced normal modes outside the frequency range investigated in the present work, in agreement with the results reported for CV dissolved in aqueous solution.³¹

The experimental results are compared with ab initio time-dependent density functional theory (TD-DFT) calculations performed with CAM-B3LYP functional⁴⁴ and the 6-311++G(2d,2p) basis set. Interestingly, the TD-DFT calculations reported in Table 1 and the ISRS extracted displacements are in good agreement, confirming the capability of the presented approach to access the details of the excited-state PES and of the normal modes with small displacements. A detailed comparison between the ISRS experimental results and the TD-DFT calculations is reported in the Supporting Information.

In conclusion, we have investigated the ISRS response in the presence of an off-resonant RP and a broadband resonant PP. A diagrammatic treatment of the pathways concurring with the signal generation has been employed to analyze the data. Taking advantage of the heterodyne background and fluorescence-free detection generated on the broadband probe pulse, Raman excitation profiles can be recorded in a single measurement, uncovering the vibrational response of systems that cannot be accessed by spontaneous or frequency domain approaches. The interaction with the resonant PP enables the projection of the molecular density matrix to the entire vibrational manifold in the excited electronic state, resulting in the interference between quantum pathways that concur with the generation of the experimental signal. Utilizing this molecular description, we have shown how to retrieve detailed information on the dipole moments over the different recorded Raman modes. As a benchmark of the proposed theoretical model and experimental scheme, we applied the two-color ISRS setup to map the PESs of cresyl violet dissolved in methanol, determining the nuclear displacements of excited-state PESs along the different monitored normal modes. Furthermore, our results establish a convenient experimental protocol, based on the use of a resonant chirped PP, to enhance the ISRS cross section of low scattering Raman modes. This protocol can be exploited for the identification of

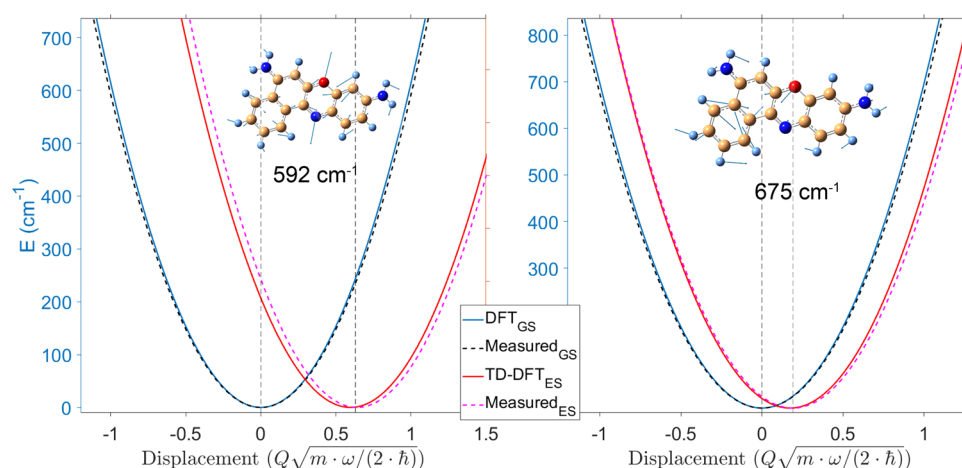


Figure 5. Cresyl violet potential energy surfaces along two normal modes (592 and 675 cm⁻¹) measured by mapping the ISRS Raman excitation profiles. The experimental results are compared with time-dependent density functional theory calculations performed with CAM-B3LYP functional and the 6-311++G(2d,2p) basis set. The vertical dashed lines indicate the measured minima of ground- and excited-state parabolas. The excited-state potentials are vertically offset by a constant factor.

mode displacements for PESs involved in relaxation dynamics, being relevant for accessing the reaction coordinates that rule the initial stages of photoreactions. Upon adding an actinic pump beam, our approach can indeed be extended in a straightforward fashion for mapping the relative orientation between different excited transient PESs.

METHODS

Experimental Setup. The experimental setup exploited for the measurements is based on a 1 kHz repetition rate Ti:sapphire laser source that generates 3.5 mJ, 35 fs pulses at 800 nm. The vertically polarized RP is synthesized by a noncollinear optical parametric amplifier (NOPA) that produces 15 fs broadband pulses centered at 680 nm, and its compression is controlled by a pair of chirped mirrors.⁴⁵ The 10 nJ vertically polarized probe pulse is a white light continuum¹⁰ generated by focusing part of the source pulse on a sapphire plate and filtering the 800 nm component by means of a short-pass filter. The PP chirp can be reduced by a second pair of chirped mirrors or increased by introducing glass windows of different widths along the beam path. Both the pulses are focused on a 500 μm glass cuvette containing the cresyl violet solution, and then the transmitted PP is frequency dispersed by a spectrometer onto a CCD device. A synchronized chopper at 500 Hz blocks alternating RP pulses in order to measure the transmitted PP in both the presence and absence of the RP excitation. In such a way, the ISRS signal $S(\omega, \Delta T)$ can be extracted as the normalized difference between the transmitted PP spectrum in the presence ($I_{\text{RP-on}}(\omega, \Delta T)$) and in the absence ($I_{\text{RP-off}}(\omega)$) of the RP:

$$S(\omega) = \frac{I_{\text{On}}(\omega, \Delta T) - I_{\text{Off}}(\omega)}{I_{\text{Off}}(\omega)}$$

The measurement of the PP chirp and the calibration of the C_2 and C_3 terms in eq 3 can be obtained monitoring both the coherent artifact generated inside the sample as well as the slope of the coherent oscillations recorded in the time domain due to the 1040 cm^{-1} Raman mode of the solvent (details are reported in the Supporting Information). Taking advantage of the small period of such a mode (~ 30 fs) this approach represents a convenient way to measure the probe pulse chirp simultaneously with the ISRS measurement. In addition, the chirp is directly measured in the very same spatial region where the ISRS signal is generated, hence directly taking into account the dispersion of the probe pulse during the propagation in the sample cuvette. Further details on the chirp calibration are reported in refs 15 and 40. The ISRS spectra of CV have been acquired for a 6.5 ps temporal window (ΔT spans from -0.5 to 6 ps), much higher than the dephasing time of the vibrational coherences (< 3 ps for all the modes under consideration), with a 13 fs sampling interval. Further details on the experimental scheme are reported in ref 46.

Density Functional Theory Calculations. DFT and TD-DFT calculations reported in Figure 5 have been performed with the CAM-B3LYP⁴⁴ functional and 6-311++G(2d,2p) basis set by using the Gaussian 09 software package. Upon optimization of the ground-state geometry by DFT, the normal mode eigenvectors calculated in the ground state have been exploited to generate displaced geometries along the normal modes under consideration, which in turn have been exploited to calculate the excited-state electronic potential by TD-DFT,

with the same level of theory. Further details are provided in the Supporting Information.

ASSOCIATED CONTENT

Supporting Information

The Supporting Information is available free of charge at <https://pubs.acs.org/doi/10.1021/acs.jpcllett.1c02209>.

Cresyl violet ISRS spectra obtained with a negatively chirped probe pulse; detailed derivation of the ISRS signals; details of the DFT and TD-DFT calculations; details of the calibration of the PP chirp; absorption spectrum of CV (PDF)

AUTHOR INFORMATION

Corresponding Authors

Giovanni Batignani – Dipartimento di Fisica, Università di Roma “La Sapienza”, Roma I-00185, Italy; Istituto Italiano di Tecnologia, Center for Life Nano Science @Sapienza, Roma I-00161, Italy; orcid.org/0000-0002-6214-8604; Email: giovanni.batignani@uniroma1.it

Tullio Scopigno – Dipartimento di Fisica, Università di Roma “La Sapienza”, Roma I-00185, Italy; Istituto Italiano di Tecnologia, Center for Life Nano Science @Sapienza, Roma I-00161, Italy; orcid.org/0000-0002-7437-4262; Email: tullio.scopigno@uniroma1.it

Authors

Carlotta Sansone – Dipartimento di Fisica, Università di Roma “La Sapienza”, Roma I-00185, Italy

Carino Ferrante – Dipartimento di Fisica, Università di Roma “La Sapienza”, Roma I-00185, Italy; Istituto Italiano di Tecnologia, Center for Life Nano Science @Sapienza, Roma I-00161, Italy; orcid.org/0000-0002-6391-0672

Giuseppe Fumero – Dipartimento di Fisica, Università di Roma “La Sapienza”, Roma I-00185, Italy; orcid.org/0000-0001-6836-8475

Shaul Mukamel – Department of Chemistry, University of California, Irvine, California 92623, United States; orcid.org/0000-0002-6015-3135

Complete contact information is available at: <https://pubs.acs.org/doi/10.1021/acs.jpcllett.1c02209>

Notes

The authors declare no competing financial interest.

ACKNOWLEDGMENTS

G.B. and T.S. acknowledge the “Progetti di Ricerca Medi 2019” grant by Sapienza Università di Roma and the “MESPEs: Mapping Excited State Potential Energy Surfaces” project by Italian Super Computing Resource Allocation. G.B. acknowledges Massimiliano Aschi for helpful support with computational resources and Emanuele Mai for constructive discussions. S.M. gratefully acknowledges the support of NSF through Grant CHE-1953045. This project has received funding from the PRIN 2017 Project, Grant No. 201795SBA3-HARVEST, and from the European Union’s Horizon 2020 research and innovation program Graphene Flagship under Grant Agreement No. 881603.

REFERENCES

(1) Zewail, A. H. Femtochemistry: Atomic-Scale Dynamics of the Chemical Bond. *J. Phys. Chem. A* **2000**, *104*, 5660–5694.

- (2) Long, D. A. *The Raman Effect*; John Wiley & Sons, Ltd., 2002.
- (3) Polli, D.; Brida, D.; Mukamel, S.; Lanzani, G.; Cerullo, G. Effective temporal resolution in pump-probe spectroscopy with strongly chirped pulses. *Phys. Rev. A: At., Mol., Opt. Phys.* **2010**, *82*, 053809.
- (4) Kuramochi, H.; Takeuchi, S.; Tahara, T. Femtosecond time-resolved impulsive stimulated Raman spectroscopy using sub-7-fs pulses: Apparatus and applications. *Rev. Sci. Instrum.* **2016**, *87*, 043107.
- (5) Liebel, M.; Schnedermann, C.; Wende, T.; Kukura, P. Principles and Applications of Broadband Impulsive Vibrational Spectroscopy. *J. Phys. Chem. A* **2015**, *119*, 9506–9517.
- (6) Mukamel, S. *Principles of Nonlinear Spectroscopy*; Oxford University Press: New York, 1995.
- (7) Potma, E. O.; Mukamel, S. In *Coherent Raman Scattering Microscopy*; Cheng, J.-X., Xie, X. S., Eds.; CRC Press: Boca Raton, FL, 2012.
- (8) Rosca, F.; Kumar, A. T. N.; Ye, X.; Sjodin, T.; Demidov, A. A.; Champion, P. M. Investigations of Coherent Vibrational Oscillations in Myoglobin. *J. Phys. Chem. A* **2000**, *104*, 4280.
- (9) Kahan, A.; Nahmias, O.; Friedman, N.; Sheves, M.; Ruhman, S. Following Photoinduced Dynamics in Bacteriorhodopsin with 7-fs Impulsive Vibrational Spectroscopy. *J. Am. Chem. Soc.* **2007**, *129*, 537–546.
- (10) Agrawal, G. *Nonlinear Fiber Optics*; Academic Press, 2013.
- (11) Kukura, P.; McCamant, D. W.; Mathies, R. A. Femtosecond Stimulated Raman Spectroscopy. *Annu. Rev. Phys. Chem.* **2007**, *58*, 461.
- (12) Batignani, G.; Bossini, D.; Di Palo, N.; Ferrante, C.; Pontecorvo, E.; Cerullo, G.; Kimel, A.; Scopigno, T. Probing ultrafast photo-induced dynamics of the exchange energy in a Heisenberg antiferromagnet. *Nat. Photonics* **2015**, *9*, 506–510.
- (13) Virga, A.; Ferrante, C.; Batignani, G.; De Fazio, D.; Nunn, A. D. G.; Ferrari, A. C.; Cerullo, G.; Scopigno, T. Coherent anti-Stokes Raman spectroscopy of single and multi-layer graphene. *Nat. Commun.* **2019**, *10*, 3658.
- (14) Batignani, G.; Pontecorvo, E.; Bossini, D.; Ferrante, C.; Fumero, G.; Cerullo, G.; Mukamel, S.; Scopigno, T. Modeling the Ultrafast Response of Two-Magnon Raman Excitations in Antiferromagnets on the Femtosecond Timescale. *Ann. Phys.* **2019**, *531*, 1900439.
- (15) Monacelli, L.; Batignani, G.; Fumero, G.; Ferrante, C.; Mukamel, S.; Scopigno, T. Manipulating Impulsive Stimulated Raman Spectroscopy with a Chirped Probe Pulse. *J. Phys. Chem. Lett.* **2017**, *8*, 966–974.
- (16) Gdor, I.; Ghosh, T.; Lioubashevski, O.; Ruhman, S. Nonresonant Raman Effects on Femtosecond Pump-Probe with Chirped White Light: Challenges and Opportunities. *J. Phys. Chem. Lett.* **2017**, *8*, 1920–1924.
- (17) Musser, A. J.; Liebel, M.; Schnedermann, C.; Wende, T.; Kehoe, T. B.; Rao, A.; Kukura, P. Evidence for conical intersection dynamics mediating ultrafast singlet exciton fission. *Nat. Phys.* **2015**, *11*, 352–357.
- (18) Fujisawa, T.; Kuramochi, H.; Hosoi, H.; Takeuchi, S.; Tahara, T. Role of Coherent Low-Frequency Motion in Excited-State Proton Transfer of Green Fluorescent Protein Studied by Time-Resolved Impulsive Stimulated Raman Spectroscopy. *J. Am. Chem. Soc.* **2016**, *138*, 3942–3945.
- (19) Kim, W.; Kim, T.; Kang, S.; Hong, Y.; Würthner, F.; Kim, D. Tracking Structural Evolution during Symmetry Breaking Charge Separation in Quadrupolar Perylene Bisimide with Time-Resolved Impulsive Stimulated Raman Spectroscopy. *Angew. Chem., Int. Ed.* **2020**, *59*, 8571.
- (20) Molesky, B. P.; Guo, Z.; Cheshire, T. P.; Moran, A. M. Perspective: Two-dimensional resonance Raman spectroscopy. *J. Chem. Phys.* **2016**, *145*, 180901.
- (21) Kuramochi, H.; Takeuchi, S.; Kamikubo, H.; Kataoka, M.; Tahara, T. Fifth-order time-domain Raman spectroscopy of photo-active yellow protein for visualizing vibrational coupling in its excited state. *Sci. Adv.* **2019**, *5*, eaau4490.
- (22) Fumero, G.; Schnedermann, C.; Batignani, G.; Wende, T.; Liebel, M.; Bassolino, G.; Ferrante, C.; Mukamel, S.; Kukura, P.; Scopigno, T. Two-Dimensional Impulsively Stimulated Resonant Raman Spectroscopy of Molecular Excited States. *Phys. Rev. X* **2020**, *10*, 011051.
- (23) Takeuchi, S.; Ruhman, S.; Tsuneda, T.; Chiba, M.; Taketsugu, T.; Tahara, T. Spectroscopic Tracking of Structural Evolution in Ultrafast Stilbene Photoisomerization. *Science* **2008**, *322*, 1073–1077.
- (24) Sun, Y.; Benabbas, A.; Zeng, W.; Kleingardner, J. G.; Bren, K. L.; Champion, P. M. Investigations of heme distortion, low-frequency vibrational excitations, and electron transfer in cytochrome c. *Proc. Natl. Acad. Sci. U. S. A.* **2014**, *111*, 6570–6575.
- (25) Johnson, P. J. M.; Halpin, A.; Morizumi, T.; Prokhorenko, V. I.; Ernst, O. P.; Miller, R. J. D. Local vibrational coherences drive the primary photochemistry of vision. *Nat. Chem.* **2015**, *7*, 980–986.
- (26) Schnedermann, C.; Muders, V.; Ehrenberg, D.; Schlesinger, R.; Kukura, P.; Heberle, J. Vibronic Dynamics of the Ultrafast all- trans to 13- cis Photoisomerization of Retinal in Channelrhodopsin-1. *J. Am. Chem. Soc.* **2016**, *138*, 4757–4762.
- (27) Batignani, G.; Fumero, G.; Kandada, A. R. S.; Cerullo, G.; Gandini, M.; Ferrante, C.; Petrozza, A.; Scopigno, T. Probing femtosecond lattice displacement upon photo-carrier generation in lead halide perovskite. *Nat. Commun.* **2018**, *9*, 1971.
- (28) Brennan, M. C.; Herr, J. E.; Nguyen-Beck, T. S.; Zinna, J.; Draguta, S.; Rouvimov, S.; Parkhill, J.; Kuno, M. Origin of the Size-Dependent Stokes Shift in CsPbBr₃ Perovskite Nanocrystals. *J. Am. Chem. Soc.* **2017**, *139*, 12201–12208.
- (29) Wang, W.; Marshall, M.; Collins, E.; Marquez, S.; Mu, C.; Bowen, K. H.; Zhang, X. Intramolecular electron-induced proton transfer and its correlation with excited-state intramolecular proton transfer. *Nat. Commun.* **2019**, *10*, 1170.
- (30) Vogel, E.; Gbureck, A.; Kiefer, W. Vibrational spectroscopic studies on the dyes cresyl violet and coumarin 152. *J. Mol. Struct.* **2000**, *550–551*, 177–190.
- (31) Leng, W.; Kelley, A. M. Resonance Raman Intensity Analysis of Cresyl Violet Bound to SiO₂ Colloidal Nanoparticles. *Langmuir* **2003**, *19*, 7049–7055.
- (32) Brazard, J.; Bizimana, L. A.; Gellen, T.; Carbery, W. P.; Turner, D. B. Experimental Detection of Branching at a Conical Intersection in a Highly Fluorescent Molecule. *J. Phys. Chem. Lett.* **2016**, *7*, 14–19.
- (33) Rafiq, S.; Scholes, G. D. Slow Intramolecular Vibrational Relaxation Leads to Long-Lived Excited-State Wavepackets. *J. Phys. Chem. A* **2016**, *120*, 6792–6799.
- (34) Batignani, G.; Ferrante, C.; Scopigno, T. Accessing Excited State Molecular Vibrations by Femtosecond Stimulated Raman Spectroscopy. *J. Phys. Chem. Lett.* **2020**, *11*, 7805–7813.
- (35) Rahav, S.; Mukamel, S. Ultrafast Nonlinear Optical Signals Viewed from the Molecule's Perspective: Kramers-Heisenberg Transition-Amplitudes versus Susceptibilities. *Adv. At., Mol., Opt. Phys.* **2010**, *59*, 223–263.
- (36) Dorfman, K. E.; Fingerhut, B. P.; Mukamel, S. Time-resolved broadband Raman spectroscopies: A unified six-wave-mixing representation. *J. Chem. Phys.* **2013**, *139*, 124113.
- (37) Batignani, G.; Fumero, G.; Mukamel, S.; Scopigno, T. Energy flow between spectral components in 2D broadband stimulated Raman spectroscopy. *Phys. Chem. Chem. Phys.* **2015**, *17*, 10454–10461.
- (38) Fumero, G.; Batignani, G.; Dorfman, K. E.; Mukamel, S.; Scopigno, T. On the Resolution Limit of Femtosecond Stimulated Raman Spectroscopy: Modelling Fifth-Order Signals with Overlapping Pulses. *ChemPhysChem* **2015**, *16*, 3438–3443.
- (39) Condon, E. U. The Franck-Condon Principle and Related Topics. *Am. J. Phys.* **1947**, *15*, 365–374.
- (40) Batignani, G.; Ferrante, C.; Fumero, G.; Scopigno, T. Broadband impulsive stimulated Raman scattering based on a chirped detection. *J. Phys. Chem. Lett.* **2019**, *10*, 7789–7796.

(41) Batignani, G.; Pontecorvo, E.; Giovannetti, G.; Ferrante, C.; Fumero, G.; Scopigno, T. Electronic resonances in broadband stimulated Raman spectroscopy. *Sci. Rep.* **2016**, *6*, 18445.

(42) Batignani, G.; Fumero, G.; Pontecorvo, E.; Ferrante, C.; Mukamel, S.; Scopigno, T. Genuine dynamics vs cross phase modulation artefacts in Femtosecond Stimulated Raman Spectroscopy. *ACS Photonics* **2019**, *6*, 492–500.

(43) Zhou, Y.; Constantine, S.; Harrel, S.; Ziegler, L. D. The probe frequency dependence of nonresonant femtosecond pump–probe nuclear responses: Undercutting vibrational inhomogeneities. *J. Chem. Phys.* **1999**, *110*, 5893–5905.

(44) Yanai, T.; Tew, D. P.; Handy, N. C. A new hybrid exchange–correlation functional using the Coulomb-attenuating method (CAM-B3LYP). *Chem. Phys. Lett.* **2004**, *393*, 51–57.

(45) Zavelani-Rossi, M.; Cerullo, G.; De Silvestri, S.; Gallmann, L.; Matuschek, N.; Steinmeyer, G.; Keller, U.; Angelow, G.; Scheuer, V.; Tschudi, T. Pulse Compression over a 170-THz Bandwidth in the Visible by Use of Only Chirped Mirrors. *Opt. Lett.* **2001**, *26*, 1155–1157.

(46) Ferrante, C.; Batignani, G.; Pontecorvo, E.; Montemiglio, L. C.; Vos, M. H.; Scopigno, T. Ultrafast dynamics and vibrational relaxation in six-coordinate heme proteins revealed by Femtosecond Stimulated Raman Spectroscopy. *J. Am. Chem. Soc.* **2020**, *142*, 2285–2292.

Excited-state energy surfaces in molecules revealed by impulsive stimulated Raman excitation profiles: Supporting Information

Giovanni Batignani,^{*,†,‡} Carlotta Sansone,[†] Carino Ferrante,^{†,‡} Giuseppe Fumero,[†]
Shaul Mukamel,[¶] and Tullio Scopigno^{*,†,‡}

[†]*Dipartimento di Fisica, Università di Roma "La Sapienza", Roma, I-00185, Italy*

[‡]*Istituto Italiano di Tecnologia, Center for Life Nano Science @Sapienza, Roma, I-00161,
Italy*

[¶]*Department of Chemistry, University of California, Irvine, 92623, California, USA*

E-mail: giovanni.batignani@uniroma1.it; tullio.scopigno@uniroma1.it

Impulsive Stimulated Raman Spectroscopy maps

In Figure S1 we report cresyl violet ISRS spectra obtained with a negatively chirped ($C_2 = -80 \text{ fs}^2$) broadband resonant PP as a function of the time delay between Raman and probe pulses and the corresponding map in the frequency domain.

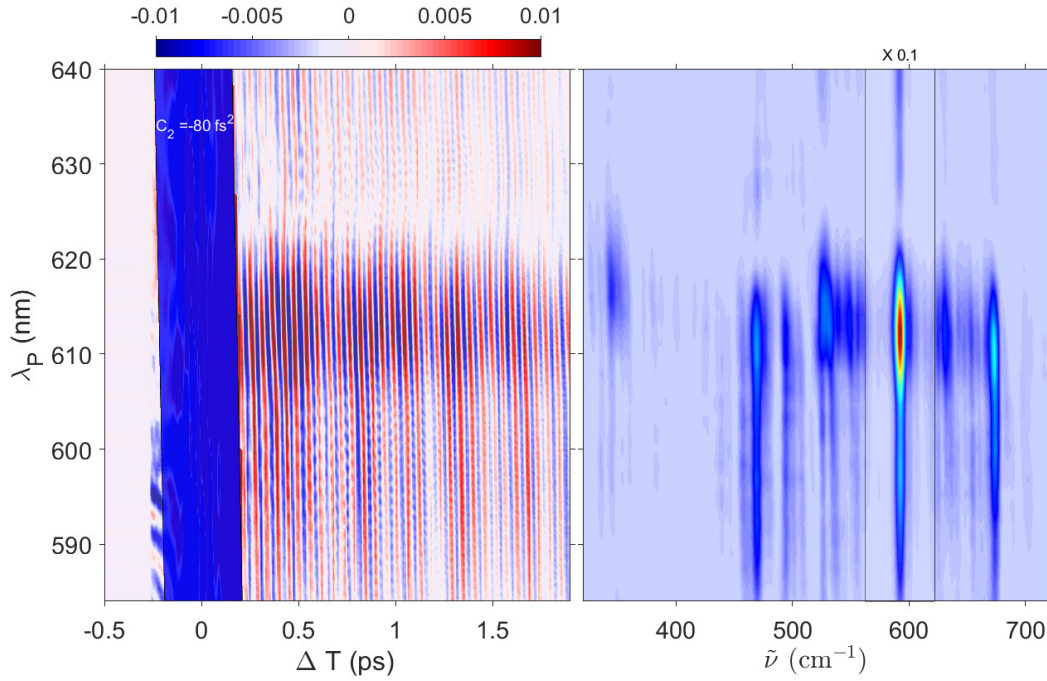


Figure S1: Cresyl Violet broadband two-color ISRS signal in time domain as a function of the probe wavelength λ_P and RP-PP relative delay ΔT (left panel) measured for a negatively chirped PP ($C_2 = -80 \text{ fs}^2$). The blue box indicates the region covered by the coherent artifact. The corresponding spectrum in the frequency domain has been obtained upon FFT and is reported in the right panel. The region around 592 cm^{-1} has been scaled by a factor 0.1 to enhance the visibility of the weaker Raman modes.

Chirp Measurement

The measurement of the PP chirp can be performed using the Coherent Artifact (CA) signal generated within the temporal overlap of two pulses, the Raman and the probe in our case,

inside the sample, identifying a wavelength dependent time delay between the two beams as

$$\tilde{\Delta T}_0(\lambda_P) = \frac{\int_{-\tau_{\lambda_s}}^{+\tau_{\lambda_s}} \Delta T |s_{CA}(\Delta T, \lambda_P)|^2 d\Delta T}{\int_{-\tau_{\lambda_s}}^{+\tau_{\lambda_s}} |s_{CA}(\Delta T, \lambda_P)|^2 d\Delta T} \quad (\text{S1})$$

where $[-\tau_{\lambda_s}, +\tau_{\lambda_s}]$ are the wavelength-dependent time window containing the CA. An alternative approach to fit the wavelength dependent delay $\tilde{\Delta T}_0(\lambda_P)$ is to exploit the time-domain ISRS signal generated by the solvent. This latter can be isolated applying a filter centered around the 1040 cm^{-1} Raman mode of the solvent to the frequency domain data and anti-Fourier transforming. The slope of the coherent oscillation in the resulting trace (reported in Fig. S2) can be exploited to extract $\tilde{\Delta T}_0(\lambda_P)$. Finally the probe chirp can be evaluated

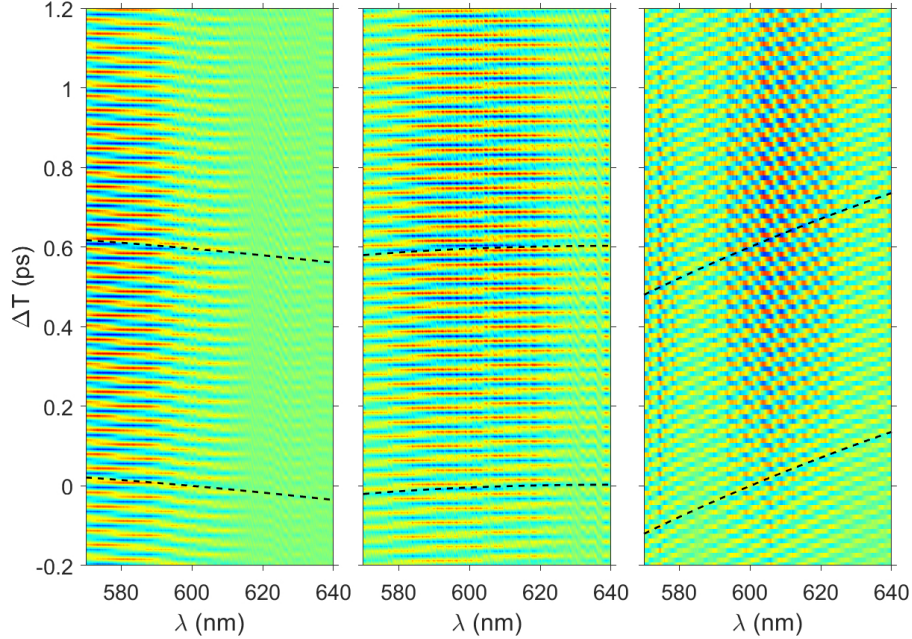


Figure S2: ISRS signal from methanol obtained upon applying a filter centered around the 1040 cm^{-1} Raman mode and anti-Fourier transforming for three different values of the probe chirp ($C_2 = -80, 40$ and 360 fs^2 , respectively). Dashed black lines show the PP chirp induced time delay $\tilde{\Delta T}_0(\lambda_P)$ between the Raman and probe pulses as a function of PP wavelength.

exploiting the relations:

$$\tilde{\Delta T}_0(\omega) = -\frac{d\phi}{d\omega}, E_P(\omega) = E_P^{(0)}(\omega)e^{i\phi(\omega)}, \phi(\omega) = \sum_n C_n(\omega - \omega_P)^n \quad (\text{S2})$$

Sample Absorption

In Fig. S3, the absorption spectrum of methanol and aqueous CV solutions are compared. Interestingly, the aqueous solution shows a blue shifted more pronounced shoulder, indicating higher displacements between the ground and the excited potential energy surfaces.

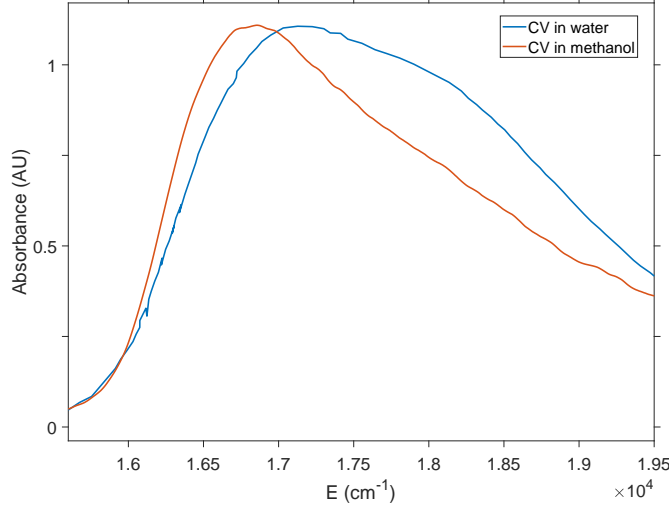


Figure S3: Absorption spectrum of Cresyl Violet dissolved in methanol is compared with the aqueous solution.¹

Derivation of the resonant ISRS signal

The third order polarization for a given vibrational mode g' can be calculated in the time domain as²⁻⁶

$$P_A^{(3)}(t) = \left(\frac{i}{\hbar}\right)^3 \sum_{e_j e_k} \mu_{ge_j} \mu_{e_j g'} \mu_{g' e_k} \mu_{e_k g} \int_0^\infty d\tau_3 \int_0^\infty d\tau_2 \int_0^\infty d\tau_1 E_R(t - \tau_1 - \tau_2 - \tau_3) E_R^*(t - \tau_2 - \tau_3) E_P(t - \tau_3) e^{-i\tilde{\omega}_{e_j g} \tau_1} e^{-i\tilde{\omega}_{g' g} \tau_2} e^{-i\tilde{\omega}_{e_k g} \tau_3} \quad (\text{S3})$$

where μ_{ij} indicate the dipole moment between the i and j states and where we have considered only exponential dephasing of the $|i\rangle\langle j|$ coherences: $\tilde{\omega}_{ij} = \omega_i - \omega_j - i\gamma_{ij}$.

More generally, considering an additional inhomogeneous dephasing function $G(\tau)$ for the electronic coherence $|e_k\rangle\langle g|$, we have

$$P_A^{(3)}(t) = \left(\frac{i}{\hbar}\right)^3 \sum_{e_j e_k} \mu_{ge_j} \mu_{e_j g'} \mu_{g' e_k} \mu_{e_k g} \int_0^\infty d\tau_3 \int_0^\infty d\tau_2 \int_0^\infty d\tau_1$$

$$E_R(t - \tau_1 - \tau_2 - \tau_3) E_R^*(t - \tau_2 - \tau_3) E_P(t - \tau_3) e^{-i\bar{\omega}_{e_j g} \tau_1} G(\tau_1) e^{-i\bar{\omega}_{g' g} \tau_2} e^{-i\bar{\omega}_{e_k g} \tau_3} G(\tau_3) \quad (\text{S4})$$

In the present work we have considered Gaussian dephasing functions $G(\tau)$ with a standard deviation equal to 330 cm^{-1} , while the Lorentzian broadening is equal to 70 cm^{-1} .

The Raman and the probe pulses in the time domain can be expressed by anti-Fourier transforming

$$E_{R/P}(t) = \int_{-\infty}^{\infty} d\omega e^{-i\omega t} E_{R/P}(\omega) \quad (\text{S5})$$

as a function of their representation in the frequency domain:

$$E_R(\omega) = E_R^{(0)}(\omega) e^{-i\omega_R \Delta T}, \quad E_P(\omega) = E_P^{(0)}(\omega) e^{i \sum_n C_n (\omega - \omega_P)^n} \quad (\text{S6})$$

where $E_R^{(0)}(\omega)$ and $E_P^{(0)}(\omega)$ are the square of the RP-PP spectra, respectively. By Fourier transforming Eq. S4 over t , we can obtain the third order nonlinear polarization in the frequency domain, which reads as

$$P_A^{(3)}(\omega) = \left(\frac{i}{\hbar}\right)^3 \sum_{e_j e_k} \mu_{ge_j} \mu_{e_j g'} \mu_{g' e_k} \mu_{e_k g} \int_{-\infty}^{\infty} dt e^{i\omega t} \int_{-\infty}^{\infty} d\omega_3 \int_{-\infty}^{\infty} d\omega_2 \int_{-\infty}^{\infty} d\omega_1$$

$$E_P(\omega_3) E_R^*(\omega_2) E_R(\omega_1) \int_0^\infty d\tau_3 \int_0^\infty d\tau_2 \int_0^\infty d\tau_1$$

$$e^{-i\omega_1(t - \tau_1 - \tau_2 - \tau_3)} e^{i\omega_2(t - \tau_2 - \tau_3)} e^{-i\omega_3(t - \tau_3)} e^{-i\bar{\omega}_{e_j g} \tau_1} G(\tau_1) e^{-i\bar{\omega}_{g' g} \tau_2} e^{-i\bar{\omega}_{e_k g} \tau_3} G(\tau_3) \quad (\text{S7})$$

Expressing also the inhomogeneous dephasing function in terms of their representation in

the frequency domain $G(\tau_1) = \int_{-\infty}^{\infty} d\omega_{D_1} e^{-i\omega_{D_1}\tau_1} G(\omega_{D_1})$, we obtain

$$\begin{aligned}
P_A^{(3)}(\omega) &= \left(\frac{i}{\hbar}\right)^3 \sum_{e_j e_k} \mu_{ge_j} \mu_{e_j g'} \mu_{g' e_k} \mu_{e_k g} \int_{-\infty}^{\infty} dt e^{i\omega t} \int_{-\infty}^{\infty} d\omega_3 \int_{-\infty}^{\infty} d\omega_2 \int_{-\infty}^{\infty} d\omega_1 \int_{-\infty}^{\infty} d\omega_{D_1} \int_{-\infty}^{\infty} d\omega_{D_3} \\
&\quad E_P(\omega_3) E_R^*(\omega_2) E_R(\omega_1) G(\omega_{D_1}) G(\omega_{D_3}) \int_0^{\infty} d\tau_3 \int_0^{\infty} d\tau_2 \int_0^{\infty} d\tau_1 \\
&\quad e^{-i\omega_1(t-\tau_1-\tau_2-\tau_3)} e^{i\omega_2(t-\tau_2-\tau_3)} e^{-i\omega_3(t-\tau_3)} e^{-i(\tilde{\omega}_{e_j g} + \omega_{D_1})\tau_1} e^{-i\tilde{\omega}_{g' g}\tau_2} e^{-i(\tilde{\omega}_{e_k g} + \omega_{D_3})\tau_3} \quad (S8)
\end{aligned}$$

By integrating over t , τ_1 , τ_2 and τ_3 , we have

$$\begin{aligned}
P_A^{(3)}(\omega) &= \left(\frac{i}{\hbar}\right)^3 \sum_{e_j e_k} \mu_{ge_j} \mu_{e_j g'} \mu_{g' e_k} \mu_{e_k g} \int_{-\infty}^{\infty} d\omega_3 \int_{-\infty}^{\infty} d\omega_2 \int_{-\infty}^{\infty} d\omega_1 \int_{-\infty}^{\infty} d\omega_{D_1} \int_{-\infty}^{\infty} d\omega_{D_3} \\
&\quad G(\omega_{D_1}) G(\omega_{D_3}) E_P(\omega_3) E_R^*(\omega_2) E_R(\omega_1) \delta(\omega - \omega_1 + \omega_2 - \omega_3) \\
&\quad \frac{-1}{-i(\tilde{\omega}_{e_k g} + \omega_{D_3} - \omega_1 + \omega_2 - \omega_3)} \frac{-1}{-i(\tilde{\omega}_{g' g} - \omega_1 + \omega_2)} \frac{-1}{-i(\tilde{\omega}_{e_j g} + \omega_{D_1} - \omega_1)} \quad (S9)
\end{aligned}$$

where the $\delta(\omega - \omega_1 + \omega_2 - \omega_3)$ represents the energy conservation and can be exploited to solve the integral over ω_3 :

$$\begin{aligned}
P_A^{(3)}(\omega) &= \left(\frac{1}{\hbar}\right)^3 \sum_{e_j e_k} \mu_{ge_j} \mu_{e_j g'} \mu_{g' e_k} \mu_{e_k g} \int_{-\infty}^{\infty} d\omega_2 \int_{-\infty}^{\infty} d\omega_1 \int_{-\infty}^{\infty} d\omega_{D_1} \int_{-\infty}^{\infty} d\omega_{D_3} \\
&\quad \frac{G(\omega_{D_1}) G(\omega_{D_3}) E_P(\omega - \omega_1 + \omega_2) E_R^*(\omega_2) E_R(\omega_1)}{(\tilde{\omega}_{e_k g} + \omega_{D_3} - \omega)(\tilde{\omega}_{g' g} - \omega_1 + \omega_2)(\tilde{\omega}_{e_j g} + \omega_{D_1} - \omega_1)} \quad (S10)
\end{aligned}$$

that can be expressed also as

$$\begin{aligned}
P_A^{(3)}(\omega) &= \left(\frac{1}{\hbar}\right)^3 \sum_{e_j e_k} \mu_{ge_j} \mu_{e_j g'} \mu_{g' e_k} \mu_{e_k g} \int_{-\infty}^{\infty} d\omega_1 \int_{-\infty}^{\infty} d\Delta \int_{-\infty}^{\infty} d\omega_{D_1} \int_{-\infty}^{\infty} d\omega_{D_3} \\
&\quad \frac{G(\omega_{D_1}) G(\omega_{D_3}) E_P(\omega - \Delta) E_R^*(\omega_1 - \Delta) E_R(\omega_1)}{(\tilde{\omega}_{e_j g} + \omega_{D_1} - \omega_1)(\tilde{\omega}_{g' g} - \Delta)(\tilde{\omega}_{e_k g} + \omega_{D_3} - \omega)} \quad (S11)
\end{aligned}$$

introducing the new variable $\Delta = \omega_1 - \omega_2$.

By defining the RP preparation function

$$I_A(\Delta) = \sum_{e_j} \mu_{ge_j} \mu_{e_j g'} \int_{-\infty}^{+\infty} d\omega_1 \int_{-\infty}^{\infty} d\omega_{D_1} G(\omega_{D_1}) \frac{E_R(\omega_1) E_R^*(\omega_1 - \Delta)}{(\omega_1 - \tilde{\omega}_{e_j g} - \omega_{D_1})} \quad (\text{S12})$$

$P_A^{(3)}(\omega)$ becomes

$$P_A^{(3)}(\omega) = \left(\frac{1}{\hbar}\right)^3 \sum_{e_k} \mu_{g'e_k} \mu_{e_k g} \int_{-\infty}^{\infty} d\omega_{D_3} G(\omega_{D_3}) \int_{-\infty}^{\infty} d\Delta \frac{E_P(\omega - \Delta) I_A(\Delta)}{(\tilde{\omega}_{g'g} - \Delta)(\tilde{\omega}_{e_k g} + \omega_{D_3} - \omega)} \quad (\text{S13})$$

By similar steps, the nonlinear polarization of diagram B_k can be expressed as

$$P_B^{(3)}(\omega, \Delta T) = \left(\frac{1}{\hbar}\right)^3 \sum_{e_k} \mu_{ge_k} \mu_{e_k g'} \int_{-\infty}^{+\infty} d\omega_{D_3} G(\omega_{D_3}) \quad (\text{S14})$$

$$\int_{-\infty}^{+\infty} d\Delta \frac{I_{RB}(\Delta, \Delta T) E_P(\omega + \Delta)}{(\Delta + \tilde{\omega}_{gg'}) (\tilde{\omega}_{e_k g'} + \omega_{D_3} - \omega)} \quad (\text{S15})$$

with

$$I_{RB}(\Delta, \Delta T) = \sum_{e_k} \int_{-\infty}^{+\infty} d\omega_1 \frac{\mu_{e_k g} \mu_{g'e_k} E_R^*(\omega_1, \Delta T) E_R(\omega_1 - \Delta, \Delta T)}{-\omega_1 - \tilde{\omega}_{ge_k}} \quad (\text{S16})$$

Density Functional Theory calculations

Density functional theory (DFT) and TD-DFT calculations have been performed with CAM-B3LYP⁷ functional and 6-311++G(2d,2p) basis set with the Gaussian 09 software package. The normal modes eigenvectors calculated in the ground state have been exploited to generate seven displaced geometries along the different normal modes under consideration, which have then been exploited to calculate by TD-DFT the energy in the excited electronic state. In Fig. S4, we report the extracted PES along the different normal mode projections. The circles indicate the energies obtained from DFT and TD-DFT calculations, while the colored parabolas are parabolic fits. For the excited state continuous lines have

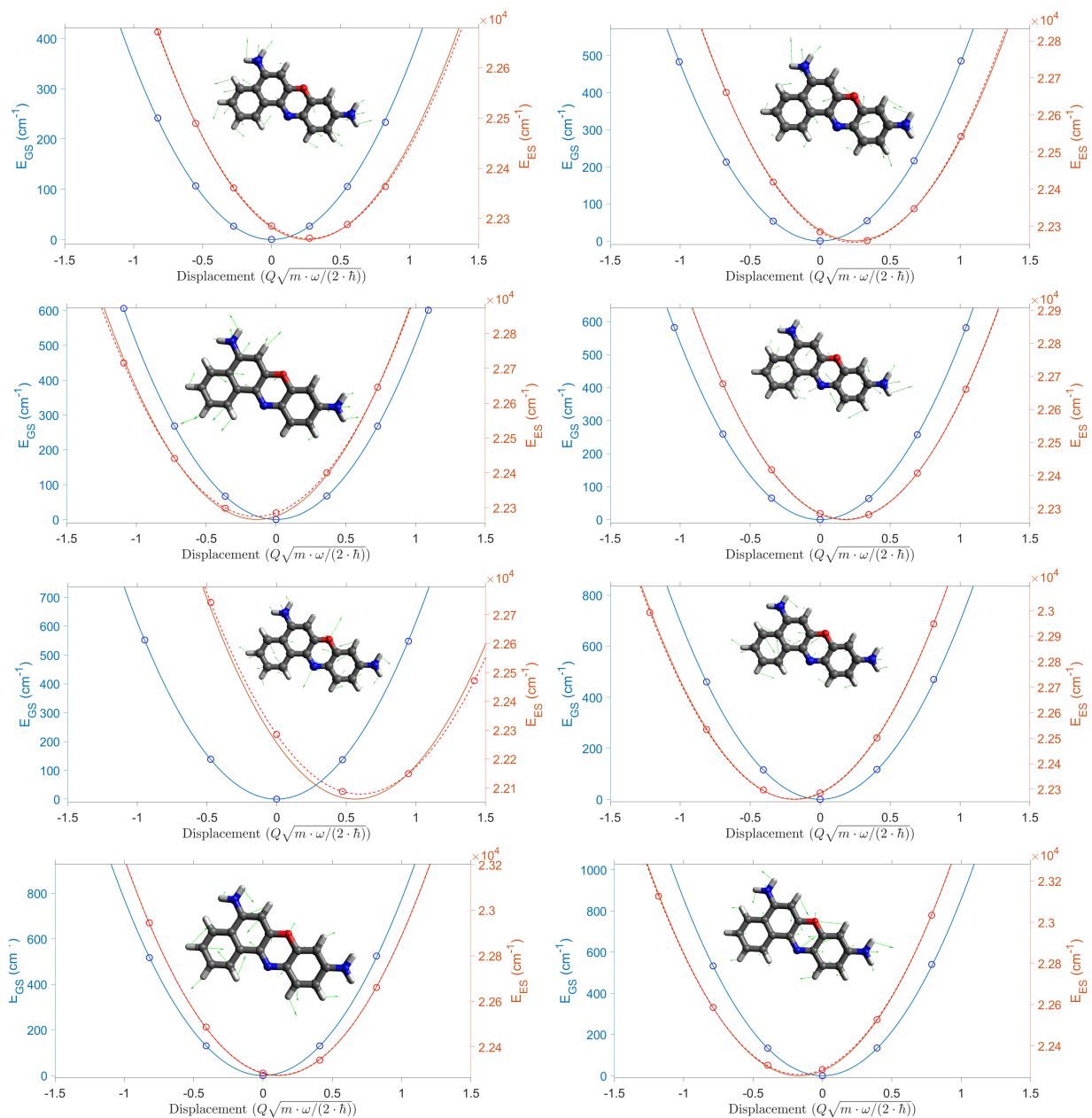


Figure S4: Potential energy surfaces, calculated using CAM-B3LYP functional and 6-311++G(2d,2p) basis set, are reported as a function of the nuclear displacement along different normal modes for the ground (blue lines) and excited (red) electronic states. The corresponding eigenvectors are reported as insets. The circles indicate the energies obtained from DFT and TD-DFT calculations, while the colored parabolas are a parabolic fit.

been extracted fixing the eigenfrequencies equal to the ground state, while for the dashed lines they have been set as a fitting parameter. In Fig. S5, the TD-DFT calculated electron density difference (EDD) map is reported in order to evaluate the relation between the electronic structure and excited state displacements. The EDD indicates a modification of the electron density in the excited state around the oxazine oxygen and nitrogen atoms, which have strong displacement along the 592 cm^{-1} normal mode (Fig. S4).

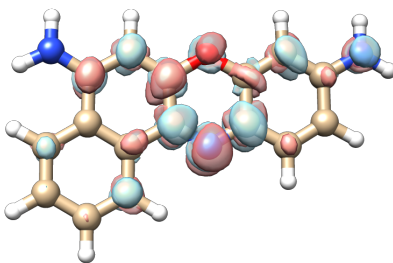


Figure S5: Electron density difference map between the ground and the excited state calculated using CAM-B3LYP functional and 6-311++G(2d,2p) basis set

Table 1: Peak positions and displacements between ground and excited state PESs are reported with the corresponding 90% confidence intervals. In the third column we report the CAM-B3LYP eigenfrequencies obtained using the CAM-B3LYP functional and the 6-311++G(2d,2p) basis set,⁷ while in the fourth one the corresponding displacements along the different normal coordinates.

| $\tilde{\nu}_{g'g}$ (cm^{-1}) | $d = Q\sqrt{\frac{m\omega_0}{2\hbar}}$ | $\tilde{\nu}^{CAM-B3LYP}$ (cm^{-1}) | $d_{CAM-B3LYP}$ |
|--|--|--|-----------------|
| 345 (2) | 0.17 (0.02) | 351 | 0.27 |
| 470 (2) | 0.20 (0.02) | 478 | 0.24 |
| 493 (2) | 0.13 (0.02) | 507 | 0.15 |
| 526 (2) | 0.26 (0.02) | 537 | 0.18 |
| 592 (2) | 0.64 (0.03) | 614 | 0.60 |
| 675 (2) | 0.19 (0.02) | 697 | 0.19 |
| 751 (2) | 0.17 (0.02) | 774 | 0.11 |
| 833 (2) | 0.17 (0.02) | 857 | 0.17 |

References

- (1) Leng, W.; Kelley, A. M. Resonance Raman Intensity Analysis of Cresyl Violet Bound to SiO₂ Colloidal Nanoparticles. *Langmuir* **2003**, *19*, 7049–7055.
- (2) Mukamel, S. *Principles of Nonlinear Spectroscopy*; Oxford University Press: New York, 1995.
- (3) Rahav, S.; Mukamel, S. Ultrafast Nonlinear Optical Signals Viewed from the Molecule's Perspective: Kramers-Heisenberg Transition-Amplitudes versus Susceptibilities. *Adv. At., Mol., Opt. Phys.* **2010**, *59*, 223–263.
- (4) Dorfman, K. E.; Fingerhut, B. P.; Mukamel, S. Time-resolved broadband Raman spectroscopies: A unified six-wave-mixing representation. *J. Chem. Phys.* **2013**, *139*, 124113.
- (5) Batignani, G.; Fumero, G.; Mukamel, S.; Scopigno, T. Energy flow between spectral components in 2D broadband stimulated Raman spectroscopy. *Phys. Chem. Chem. Phys.* **2015**, *17*, 10454–10461.
- (6) Batignani, G.; Ferrante, C.; Fumero, G.; Scopigno, T. Broadband impulsive stimulated Raman scattering based on a chirped detection. *J. Phys. Chem. Lett.* **2019**, 7789–7796.
- (7) Yanai, T.; Tew, D. P.; Handy, N. C. A new hybrid exchange–correlation functional using the Coulomb-attenuating method (CAM-B3LYP). *Chem. Phys. Lett.* **2004**, *393*, 51–57.